Chapter 4: Results

This chapter presents some of the results obtained with the present method. For convenience they will be separated into steady-state and unsteady results. The first type corresponds to unsteady calculations that converge to steady-state conditions; in all these cases boundary and operating conditions remain constant within flammability limits. The first set of steady-state results corresponds to a constant-area tube with friction; numerical calculations are compared to analytical results. The second set, corresponding to a production straight-flow combustor, is compared with calculations from an industrial one-dimensional code. The final set is for a generic reverse-flow, open-primary combustor. The unsteady results include blow-out limits for the constant-area tube introduced before. These limits are determined for given boundary conditions, and define the stability or operating region for the combustor. The time-events leading to a blow-out are also shown, for both a lean and rich blow-out. The final set of unsteady results show the response of the previously-described reverse-flow combustor to perturbations in operating and boundary conditions.

All the results presented in this chapter were obtained with a Pentium 200 desktop computer.

4.1. Steady-State Calculations

4.1.1. Comparison with Analytical Solution

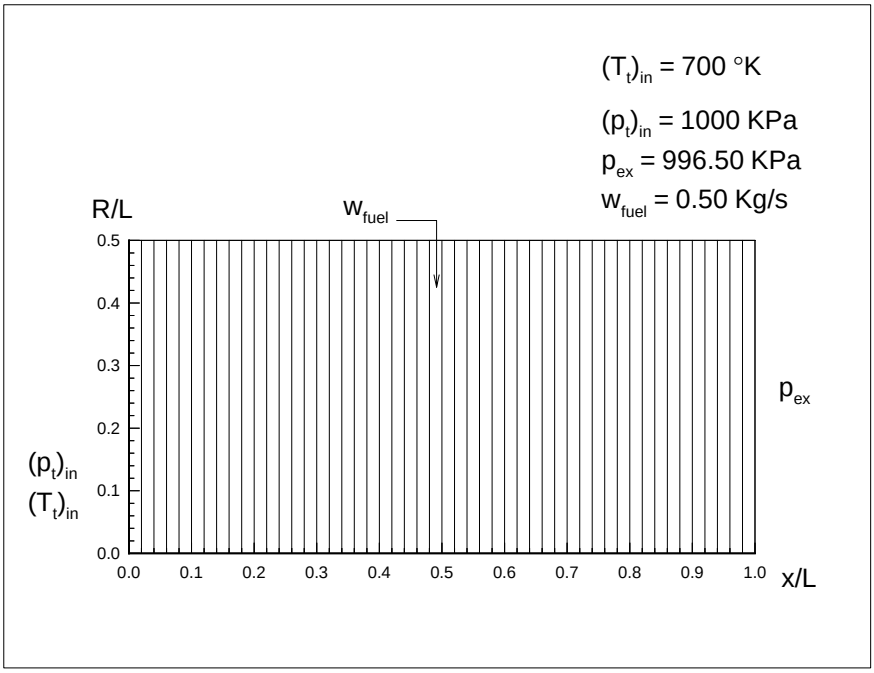

Figure 4.1: Constant-area configuration for analytical validation.

Figure 4.1 shows the configuration used for the analytical validation: a constant-area cylindrical tube around the x-axis. Also shown are the boundary and operating conditions for the simulation, resulting in an inlet flow-rate of 0.5 kg/s and an equivalence ratio of about 0.94; the fuel used was propane (C_3H_8). Not shown in the figure is a friction force along the walls of the tube equivalent to a total pressure-loss $\Delta p_t / p_t = 0.0005$ (which under these conditions is equivalent to a friction factor of about 0.05 - see equation 2.31). The length of the combustor (used in Fig. 4.1 for non-dimensionalization) was L = 0.10 m.

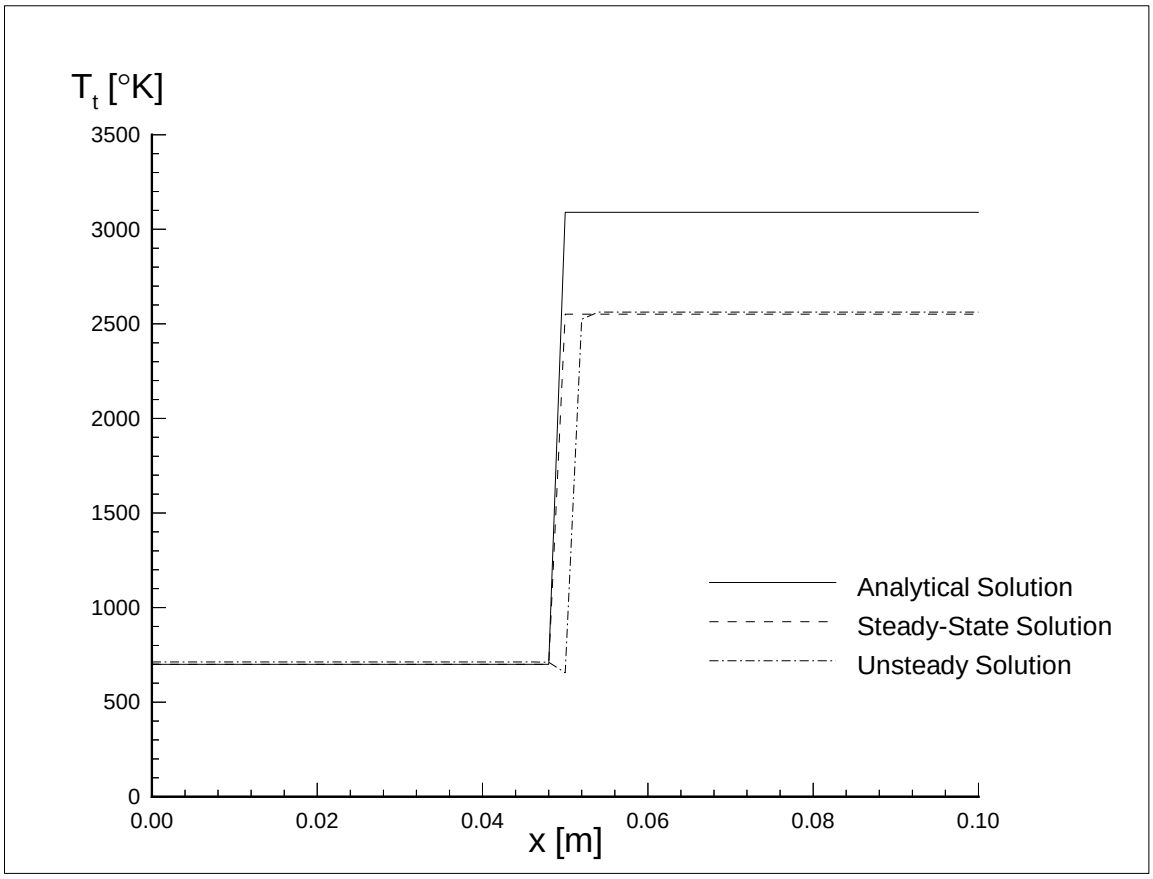

Figure 4.2: Results from the analytical validation - Temperature distribution.

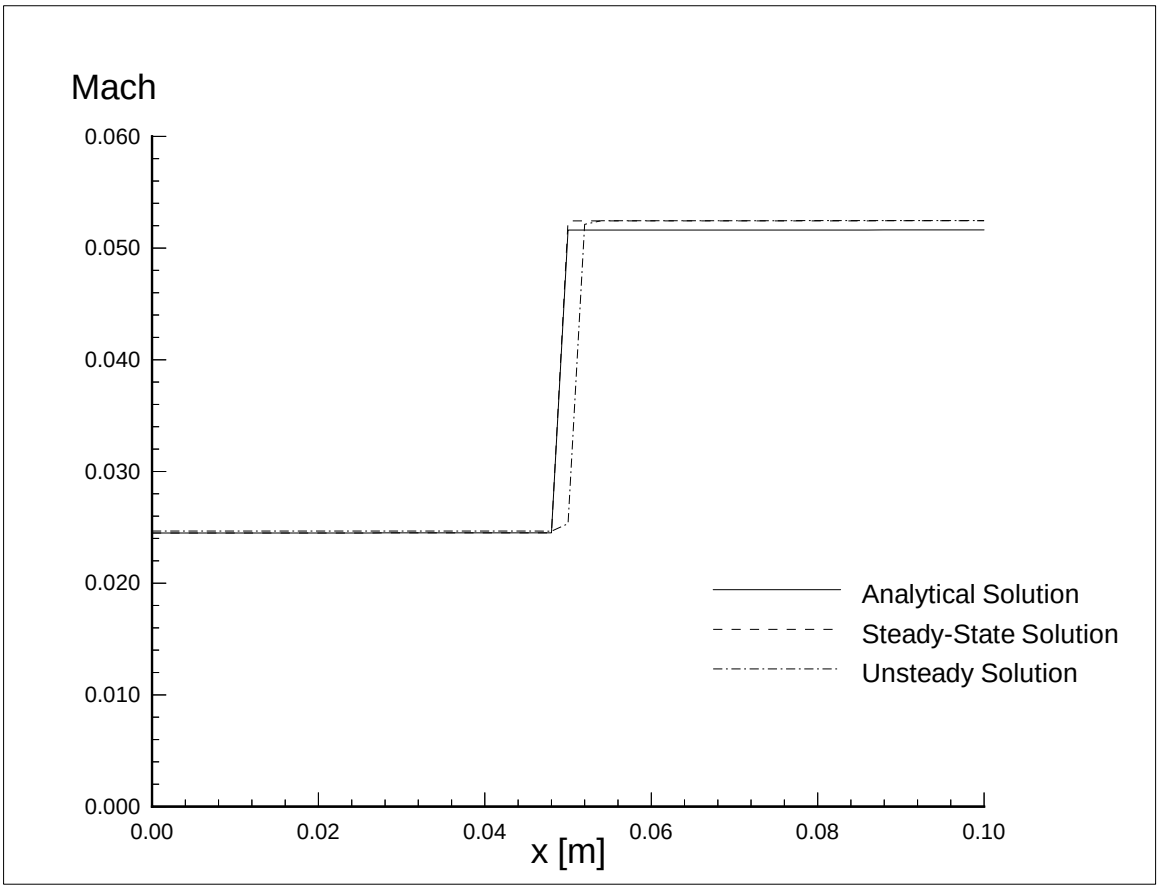

Figure 4.3: Results from the analytical validation - Mach-number distribution.

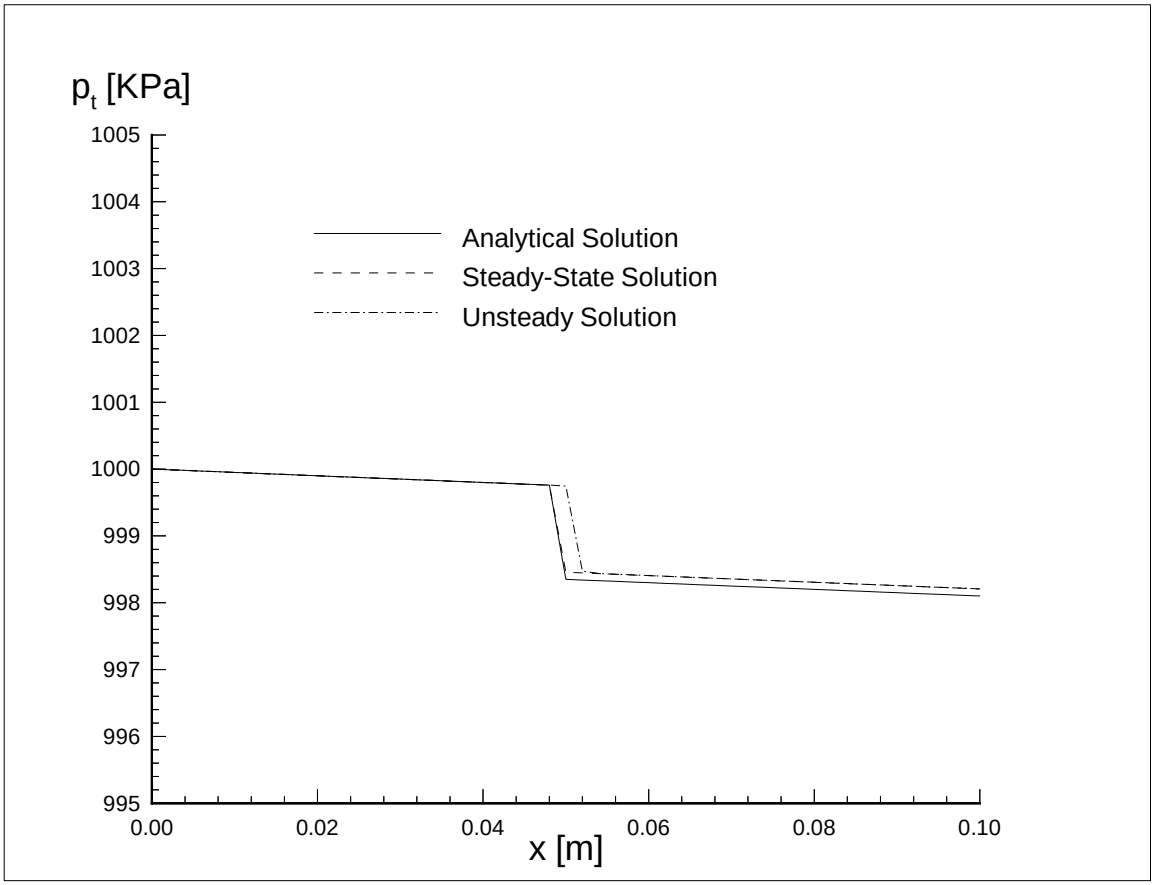

Figure 4.4: Results form the analytical validation - Total-pressure distribution.

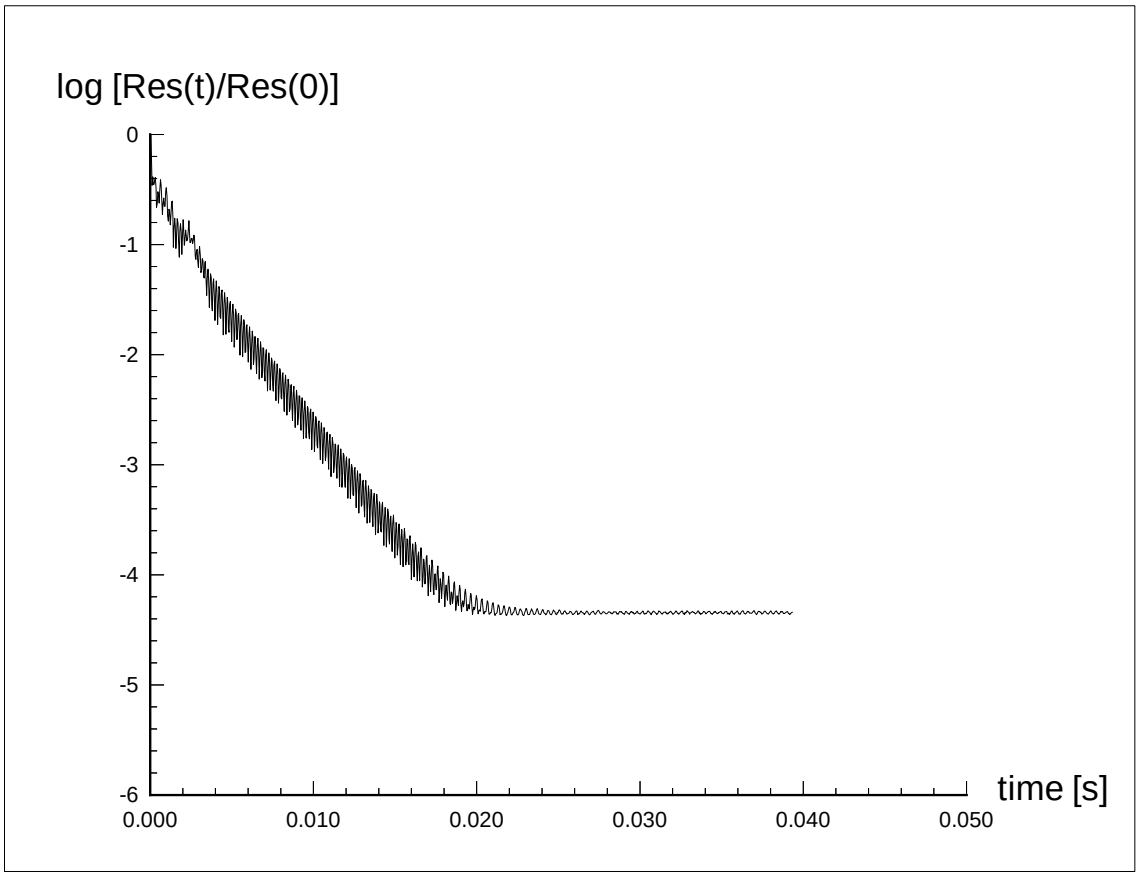

Figure 4.5: Results from the analytical validation - Convergence of the residual.

For the numerical calculations the domain was discretized in 50 CVs; the total pressure-loss was uniformly distributed among the CVs. The total number of iterations run was 2000 with a CFL number of 10. The analytical solution corresponds to a steady-state, compressible, calorically-perfect flow with friction. The resulting equations for this flow are derived in Hill and Peterson (1992).

Figures 4.2-4.5 show the results for the present case. The analytical solution is compared with the present unsteady (finite-rate) solution. Also a steady, infinite-rate solution (Rodriguez and O'Brien [1998]) used to initialize calculations is included for reference.

Figure 4.2 presents the distribution of total temperature along the combustor. The analytical solution (essentially the first law with constant specific heats) predicts a much higher temperature than either method; this can be attributed to the calorically-perfect assumption. The unsteady solution exhibits a spatial delay before the temperature rise. This is due to the finite-rate effect and the assumption that fuel enters at 300 ^{0}K, i.e., a lower temperature than the inlet flow. The Mach number distribution is shown in Fig. 4.3, and the total pressure in Fig 4.4. In both cases, all solutions are very close to each other.

The convergence of the residual is presented on Figure 4.5, in the way most common in CFD (i.e., orders of reduction in the magnitude of the square-root average sum of all the components of the residual). The maximum component (or error) corresponds to the energy equation at the fuel-input CV. Initially this component is about the same order as the input energy flux. By the time of convergence, it had been reduced four orders of magnitude to less than 0.1% of this flux.

In brief, this simple case points to the fact that the results provided by the present method at the very least satisfy a necessary condition, i.e., the ability to model a textbook case often used to produce preliminary information in heat-release environments (Hill and Peterson [1992]).

4.1.2. Straight-Flow Annular Combustor

Figure 4.6 presents an early Rolls-Royce design for a straight-flow combustor, axi-symmetric around an axis at y = 0 (not shown for clarity). Also presented are the main geometric elements, boundary and operating conditions, and the mesh used for calculations. The fuel used was Jet-A ($C_{12}H_{23}$ - see McBride et all [1993] for its thermodynamic properties).

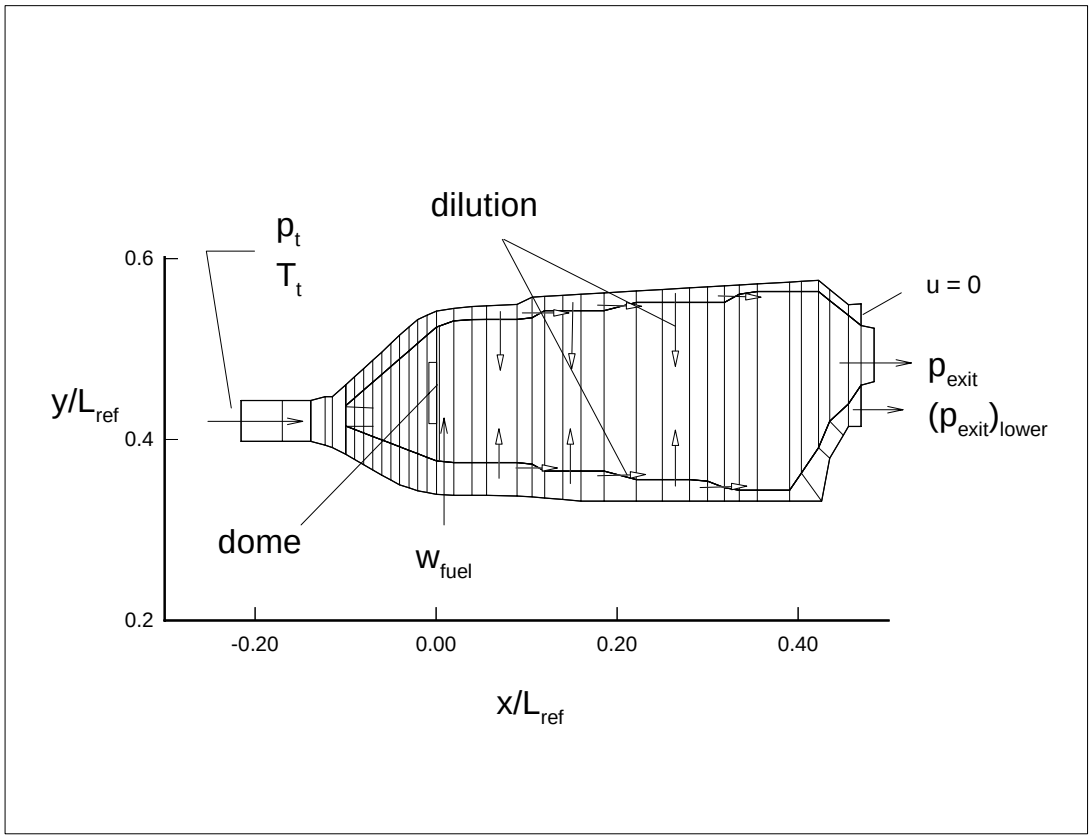

Figure 4.6: Straight-flow combustor - Configuration, discretization, and boundary and operating conditions.

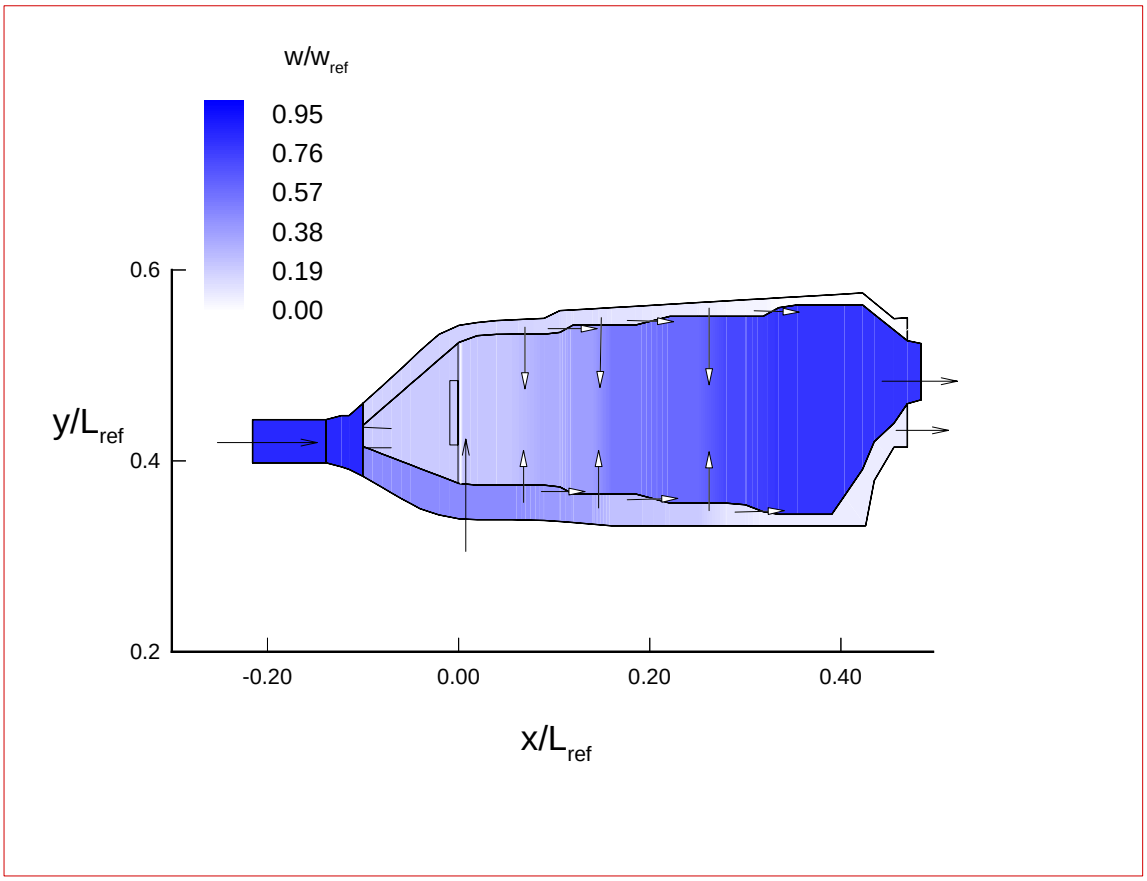

Figure 4.7: Straight-flow combustor - Contour-plot for mass flow-rate.

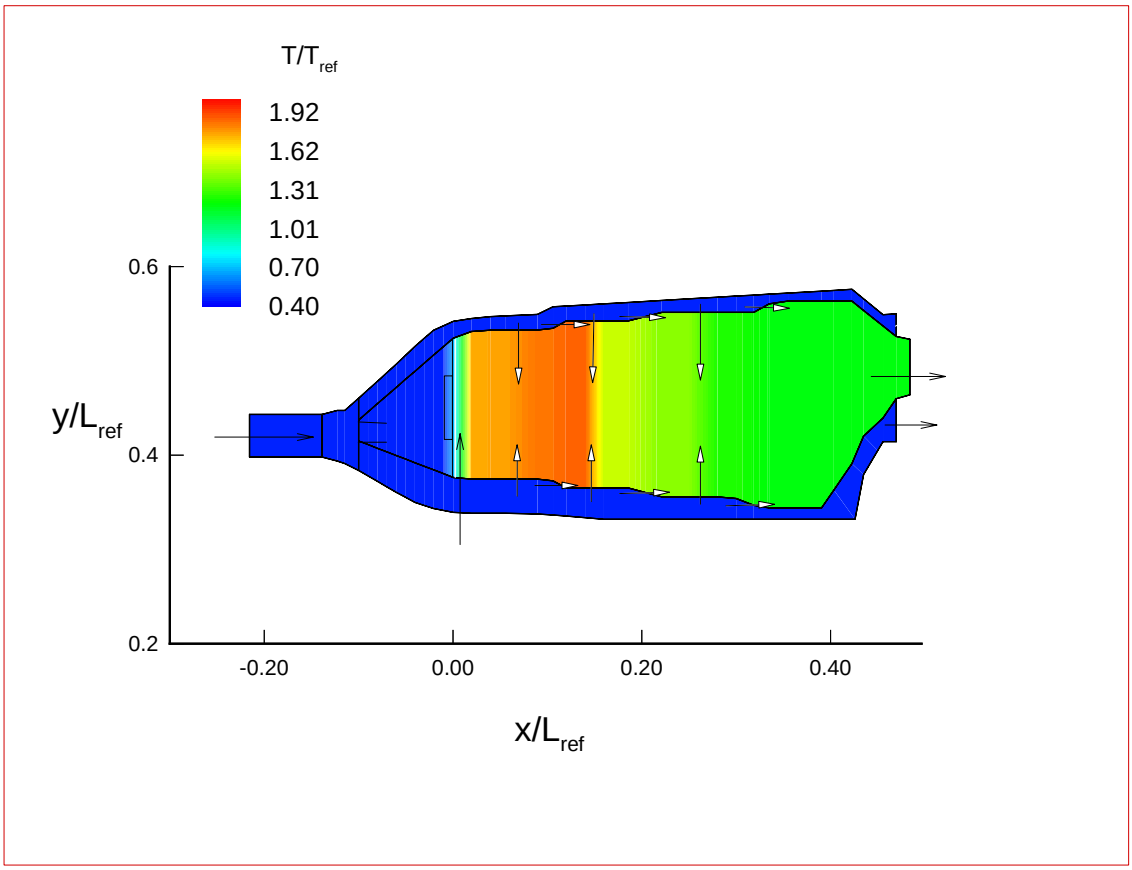

Figure 4.8: Straight-flow combustor - Contour-plot for temperature.

The present model's results for this configurations can be seen in Figures 4.7 and 4.8 in the form of contour plots for mass flow-rate and temperature. All quantities have been non-dimensionalized with reference values that are Rolls-Royce proprietary information. Figure 4.7 presents the mass flow-rate w. As can be seen, all the air coming from the inlet divides itself into the primary and annular flow-paths. Downstream from the dome air from the annular paths flows into the primary. At the end most of the flow comes out at the exit of the primary, with a small amount coming out from the lower-annular path (the upper-annular path is assumed closed - see Fig.4.6).

Figure 4.8 shows the resulting temperature distribution. Cold air occupies most of the combustor, including the annular paths and the primary region up to the dome. As the fuel-air ratio immediately following is on the rich side, the maximum temperature is reached only after air from dilution brings the mixture closer to stoichiometry (or alternatively burns the excess fuel). As more air comes into the primary region, the temperature goes down. The resulting mixture finally leaves at a temperature roughly intermediate between inlet and maximum.

These calculations were performed with the fully-implicit scheme using a CFL number of 5.0. Calculations again were initialized with an infinite-rate solution. Residual was reduced in about six orders of magnitude after 2000 iterations, in a fashion similar to the previous case. Approximate running time was 7 minutes for the discretization shown in Fig. 4.6.

In order to arrive at the results shown, additional data had to be provided to the model. This data had to do with all the sources of pressure loss that could not be handled by chemical reactions, or by the source-terms described in Section 2.10

(specifically **excluding** friction losses). In order to quantify this additional information and to validate our model with a recognized standard, comparison was made with an existing code, which is a Rolls-Royce proprietary code (and hereafter will be known as “RR code”) This is an already-validated, industrial-quality, one-dimensional combustor model. The data from this code was provided to this author in a discrete fashion and will be shown as such in subsequent figures (Weeks, 1997).

Figure 4.9 shows a comparison between the RR-code calculations and the present method, the latter without the additional losses (i.e., in an “inviscid” mode). As can be seen, without this additional information the present model can not capture the losses in the diffuser immediately before the dome, nor in the lower-annular path immediately before the first band of dilution holes. The resulting pressure distribution forced flow from the primary into the lower-annular path. The deep drop in pressure in this path signals the point where the flow choked and calculations stopped. It should be noted that RR-code calculations were aided by empirical information regarding the pressure losses in the diffuser at the inlet of the primary flow (Weeks, 1997). In any case these losses can be attributed for the most part to viscous effects. From a one-dimensional point of view they require the specification of some friction coefficient, either directly or indirectly through the pressure losses, as indicated in Section 2.10. The latter approach was followed here.

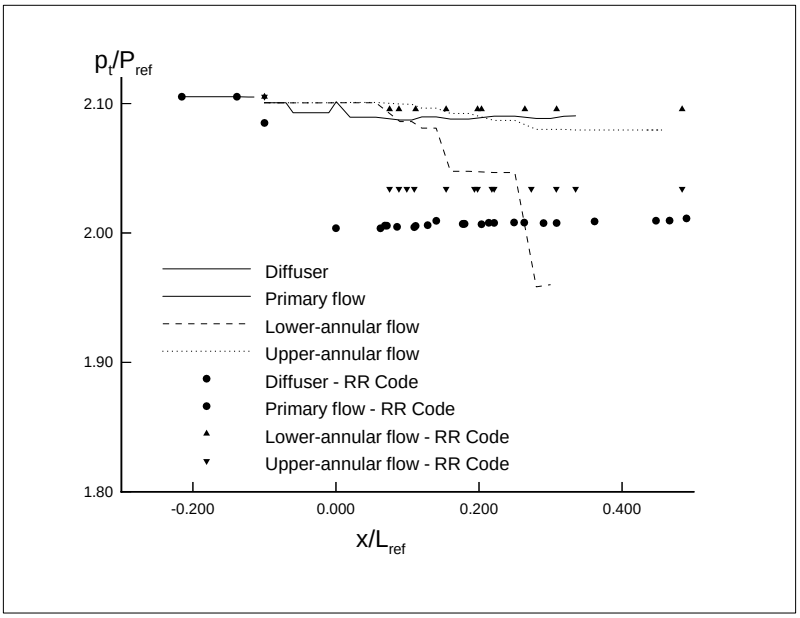

Figure 4.9: Total-pressure distribution: "inviscid" calculations.

The pressure-loss deviations from Figure 4.9, mainly the region between flow-division and reaction-zone or dilution in all paths, were fed back into the model. The resulting property distributions are presented in Figures 4.10-4.12. The first figure shows the modified pressure-loss distribution. The additional information allows the model to reach the level of total pressure predicted by the RR-code in all paths. It is interesting to note that there is a slight positive slope (i.e., total pressure **increase**) in the primary flow in both sets of calculations. At least for the present method, this is due to the transfer of axial momentum from the annular flows to the primary (i.e., the dilution flow enters at an angle with respect of the vertical). Our calculations also show pressure drops in the annulars for the same reason (the RR code predicts constant total pressure). No friction-loss estimates were included in the primary or dilution regions; predictions seem to justify their omission.

The mass flow-splits appear in Fig. 4.11. This time the “correct” pressure distribution allows for the different mass-transfers between the paths to be ade-

quately predicted. Also the total air flow-rate into the combustor is reasonably predicted. It should be taken into account that in the RR code the inlet flow-rate is given and the exit pressure calculated, while the opposite is true in the present method.

Finally, Fig. 4.12 shows the total-temperature distributions. The present calculations over-predicts the maximum temperature in the reaction zone with respect to the RR code. The latter code uses a constrained-equilibrium approach with a proprietary efficiency correlation; this correlation may account for at least some of the temperature difference (Weeks, 1997). The resulting effect of dilution appears correctly captured. It should be noted that the current model does not include any source terms for heat-transfer between the paths. That may explain the small difference at the exit of the primary with respect to the RR code.

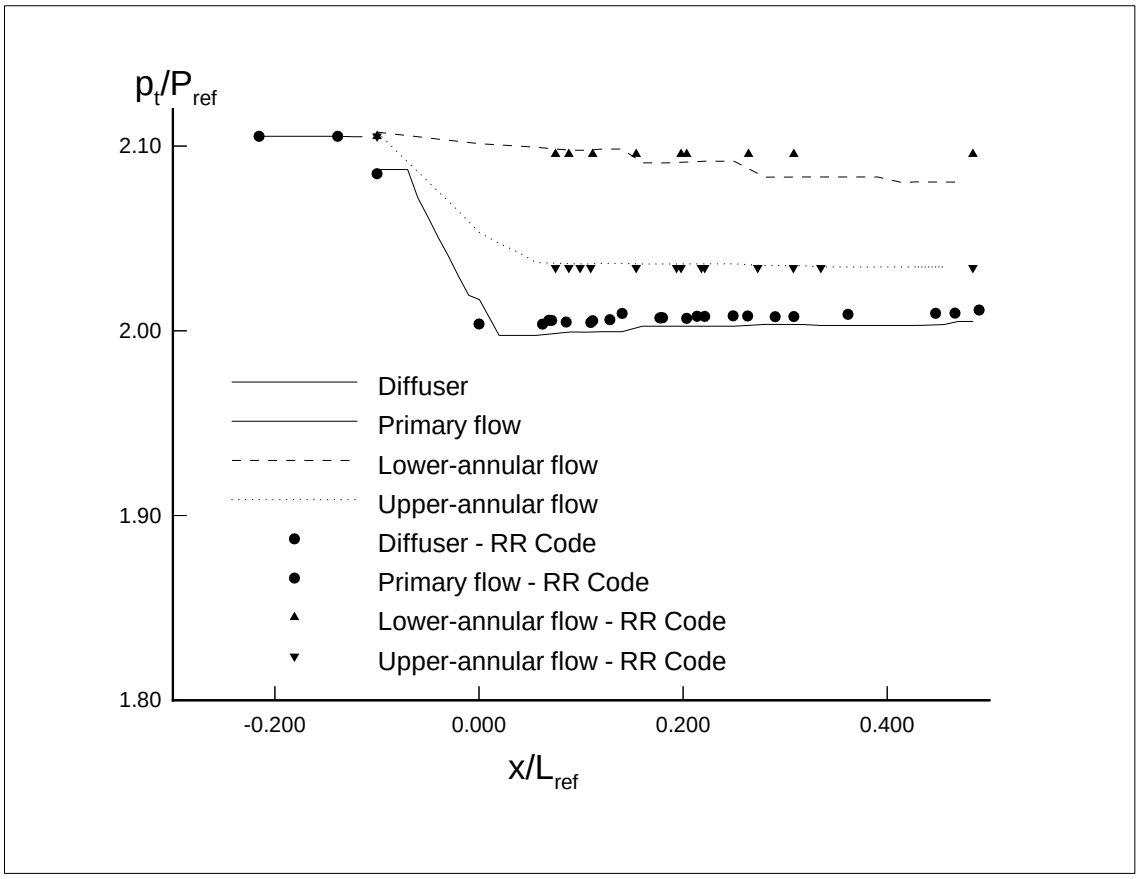

Figure 4.10: Straight-flow combustor - Total-pressure distribution.

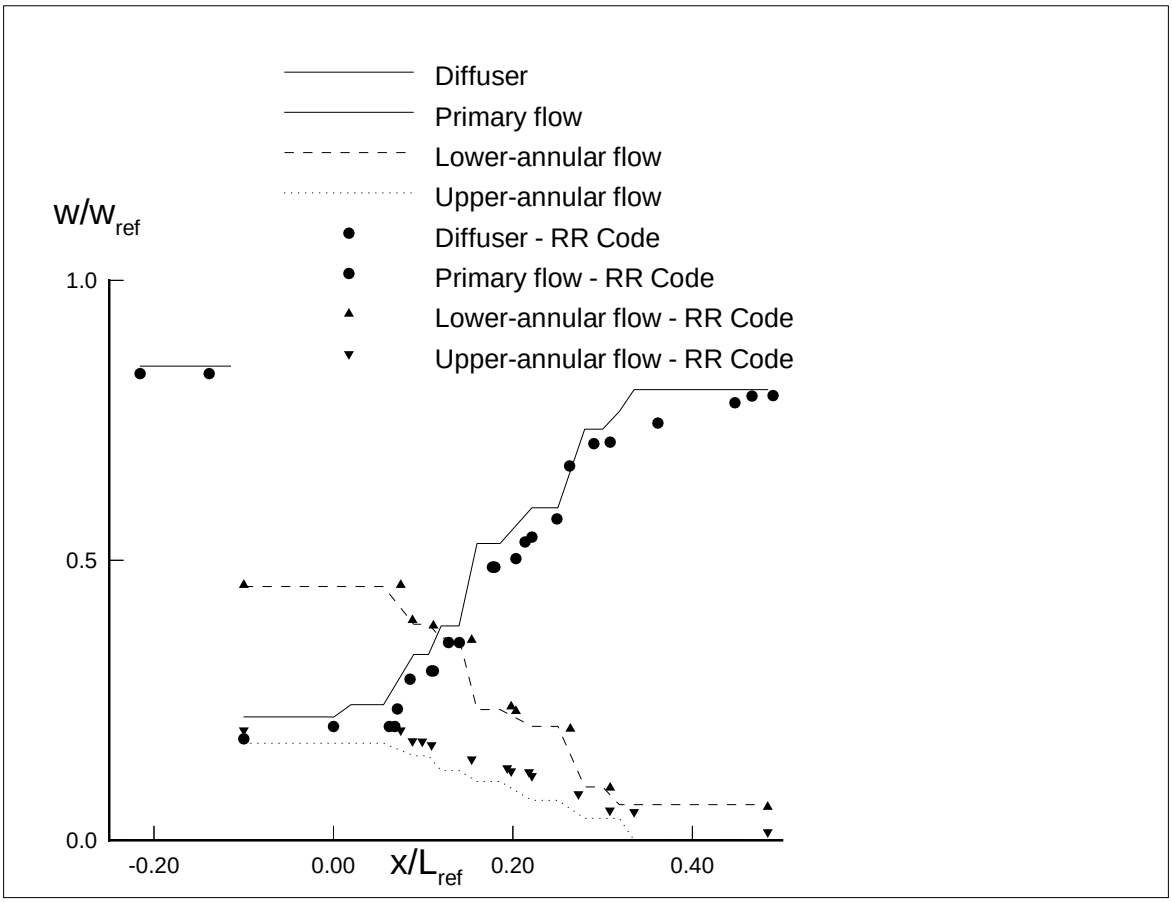

Figure 4.11: Straight-flow combustor - Mass flow-rate distribution.

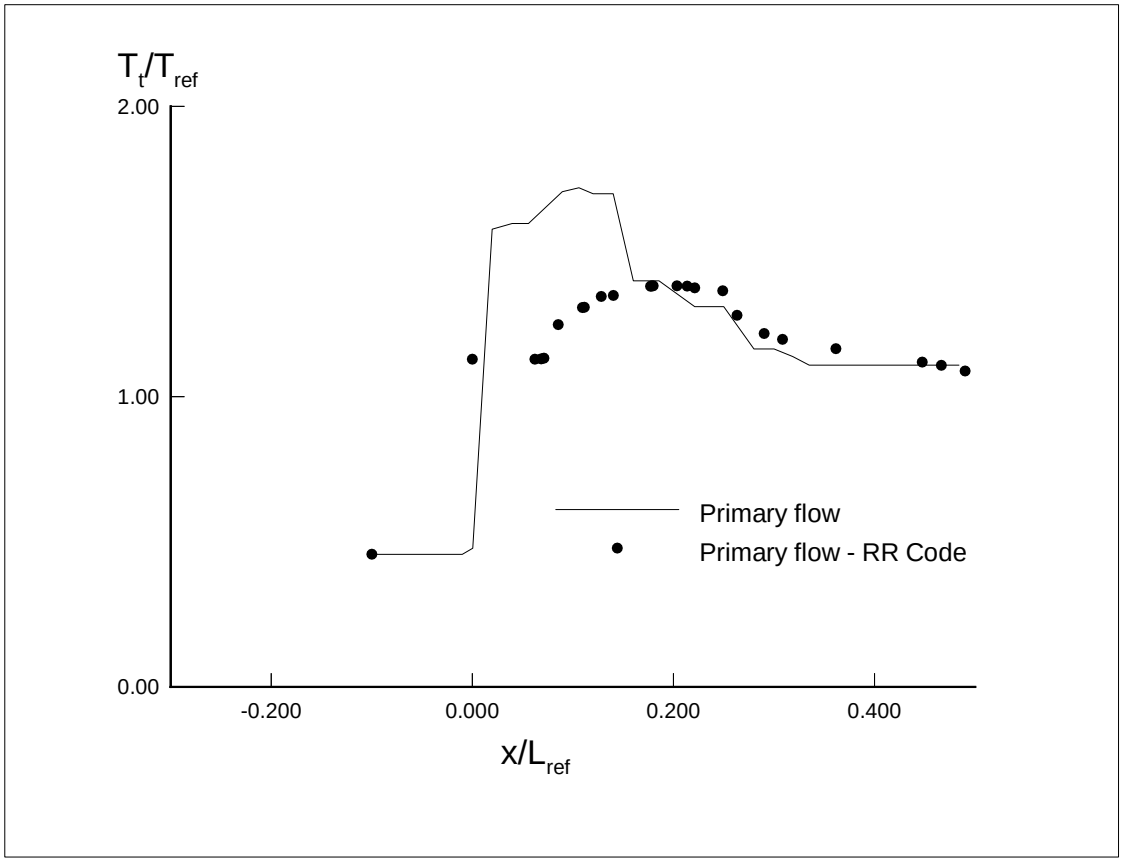

Figure 4.12: Straight-flow combustor - Total-temperature distribution.

At this point the methodology used to obtain the “correct” pressure losses may be open to question. After all, if previously-existing data (either experimental or numerical) is going to be used to “guide” the current model to the “right” solution, what is the value of the model as a predictive tool? The answer lies in the fact that a model like the present one will not be used for a single operating condition, but rather for a considerable number of them. Therefore it is expected that the model would be calibrated for one of them (like the one shown) and that this calibration will remain fixed for most other conditions. This is similar to what it is done with more sophisticated multi-dimensional codes in industrial applications (see Danis et al [1996]). Whether the approach is valid for models like the current one will be decided as more data becomes available.

4.1.3. Reverse-Flow, Open-primary Combustor

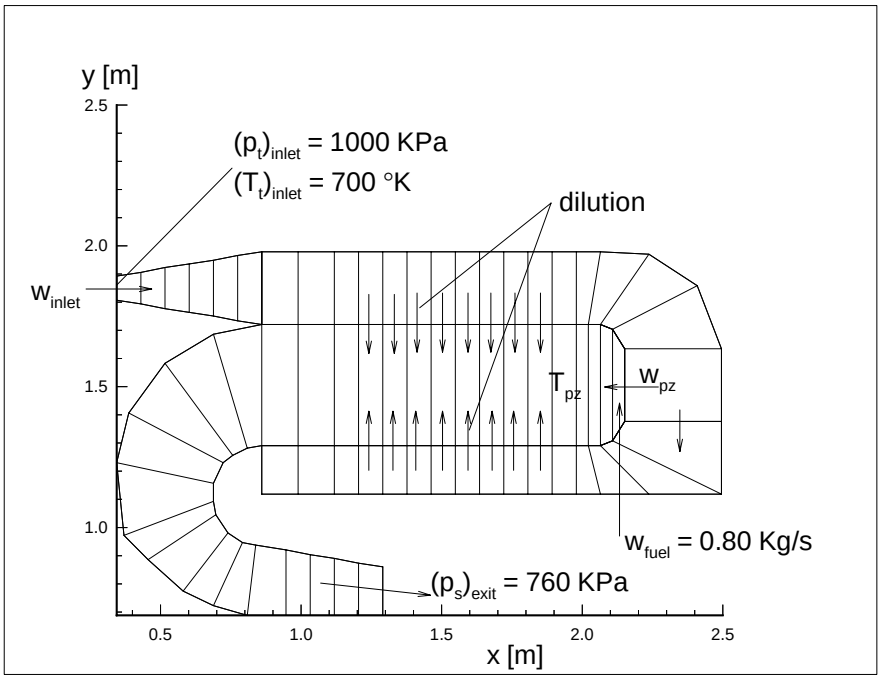

Figure 4.13: Reverse-flow, open-primary combustor configuration.

Figure 4.13 shows a generic reverse-flow, open-primary combustor, together with the boundary and operating conditions with which it was tested (the fuel was Jet-A), and the grid used for calculations. These were done with a CFL = 5.0, and the residual was reduced four orders in 1000 iterations from its infinite-rate initialization (running time approximately 3 minutes).

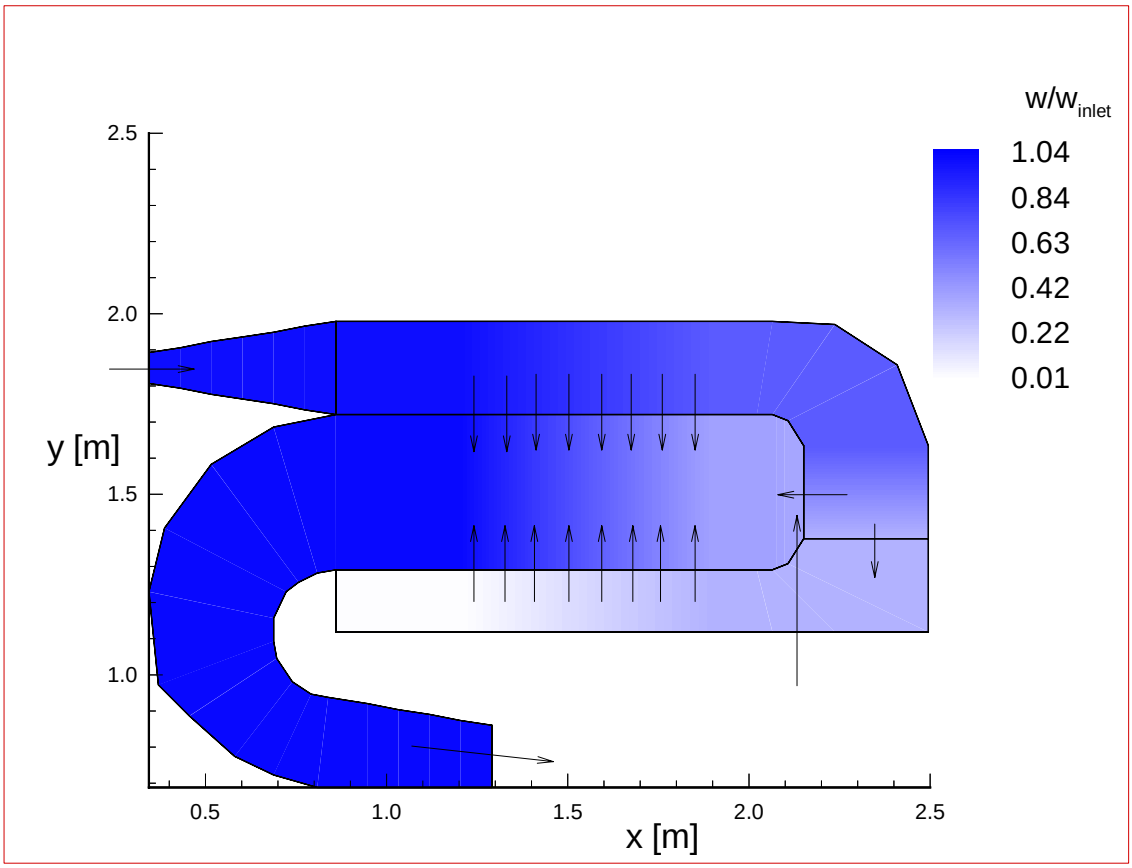

Figure 4.14: Reverse-flow combustor - Contour-plot for mass flow-rate.

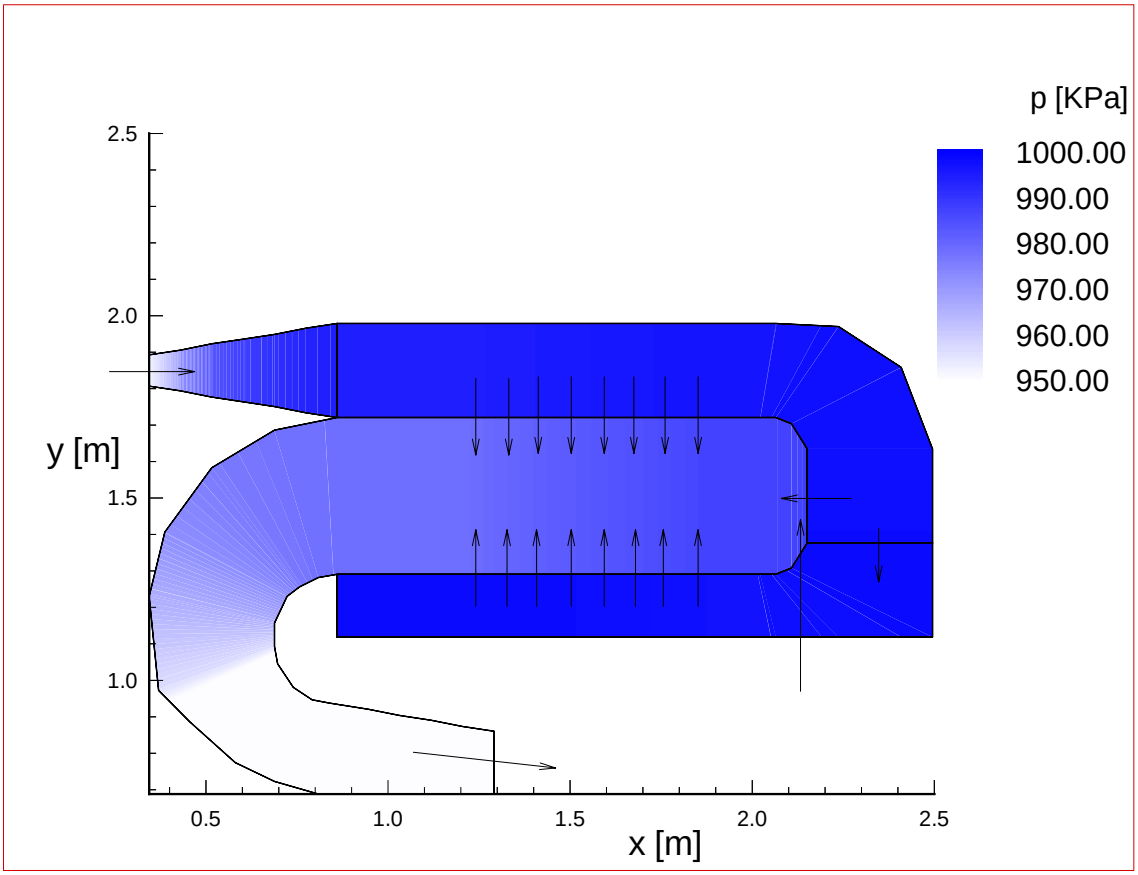

Figure 4.15: Reverse-flow combustor: Contour-plots for static pressure.

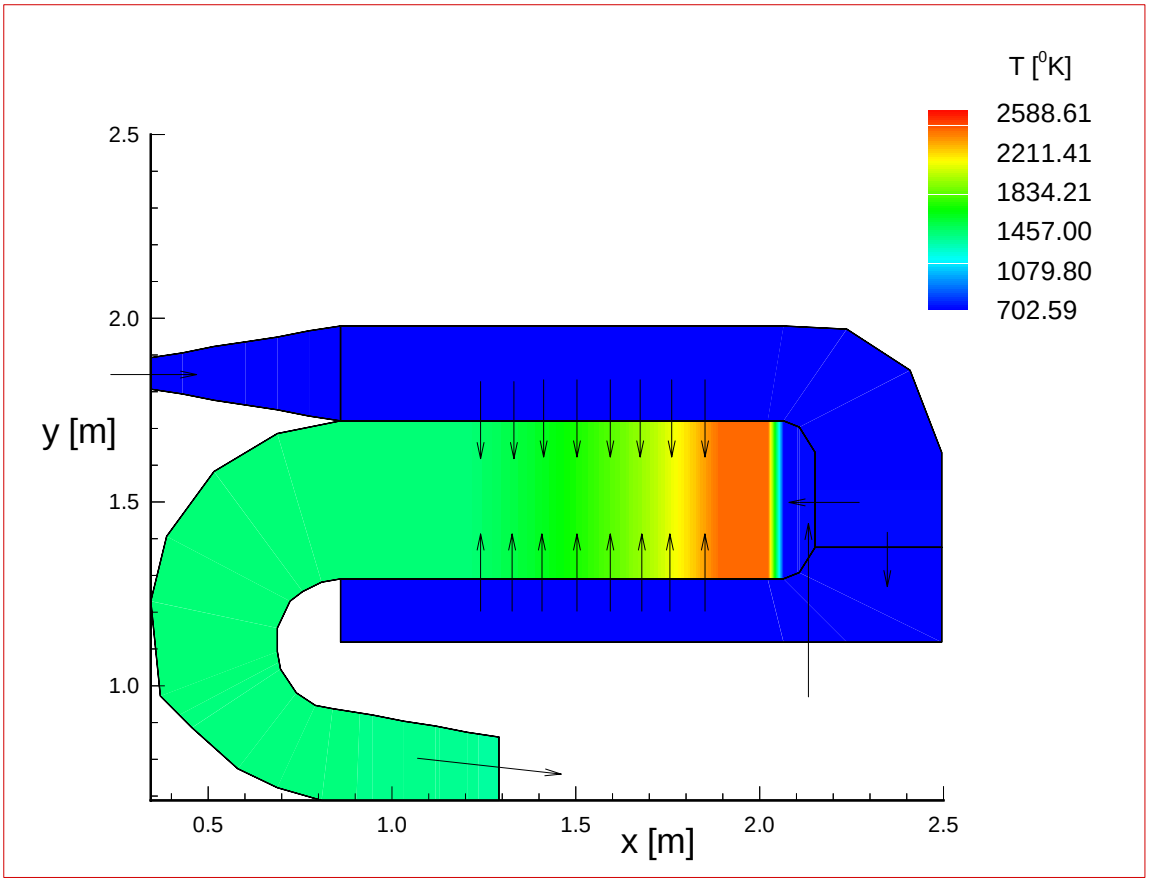

Figure 4.16: Reverse-flow combustor: Contour-plots for temperature.

The contour-plots for mass flow-splits and temperature can be seen in Figures 4.14-4.16. As in the case of the straight-flow combustor, the method captures the transfer of mass between the different paths, and the effect of dilution in the temperature distribution. No assumptions were made regarding additional pressure losses (i.e., the calculations were “inviscid”). Note the pressure scale was “cut” at 950 KPa to better show the difference in pressure between the primary and the surrounding flow-paths.

4.2. Unsteady Calculations

4.2.1. Blowout Predictions

The constant-area configuration in Fig. 4.1 was used again, this time to investigate the ability to predict flame blowout. This situation occurs when the local flame velocity is smaller than the overall mixture velocity. In this situation the flame (which represents the localized combustion zone - see Turns [1996]) is carried downstream and we end up with a flow of non-reacting mixture. The flame speed is maximum near stoichiometric conditions and decreases for both lean and rich mixtures (Turns [1996]).

For these numerical experiments the inlet total pressure and temperature were held constant at the values shown in Fig. 4.17. The domain was discretized in 100 CVs. The fuel (C_3H_8) flow-rate and the exit static pressure were varied until the desired inlet flow-rate and overall equivalence ratio were achieved. Calculations were initialized with the infinite-rate steady-state solution corresponding to the desired operating condition. Although in all cases steady-state conditions were achieved, for blowout the final solution is radically different from the initial; therefore the present case was considered “unsteady”.

Figure 4.17 shows how the blow-out limits, in the form of maximum and minimum values of equivalence-ratio ϕ change with inlet flow-rate. It is apparent that the “loop” does not close at $\phi = 1$, as it commonly occurs in the literature. Several explanations may be attempted. As the limit is approached, calculations become “unstable”, i.e., small changes in parameters, initial conditions, etc., may push results one way or the other. This is particularly true for the small inlet Mach numbers encountered here (of the order of 0.01). Furthermore the curves in Fig.

4.17 represent points where there is still a flame inside the duct and therefore do not represent actual blow-out. Finally most stability curves in the literature correspond to single “well-stirred reactors”, which assume perfect mixing. The current approach is more akin to a succession of elemental “plug-flow reactors” where there is no mixing at all (more details on these concepts can be found in Turns [1996]).

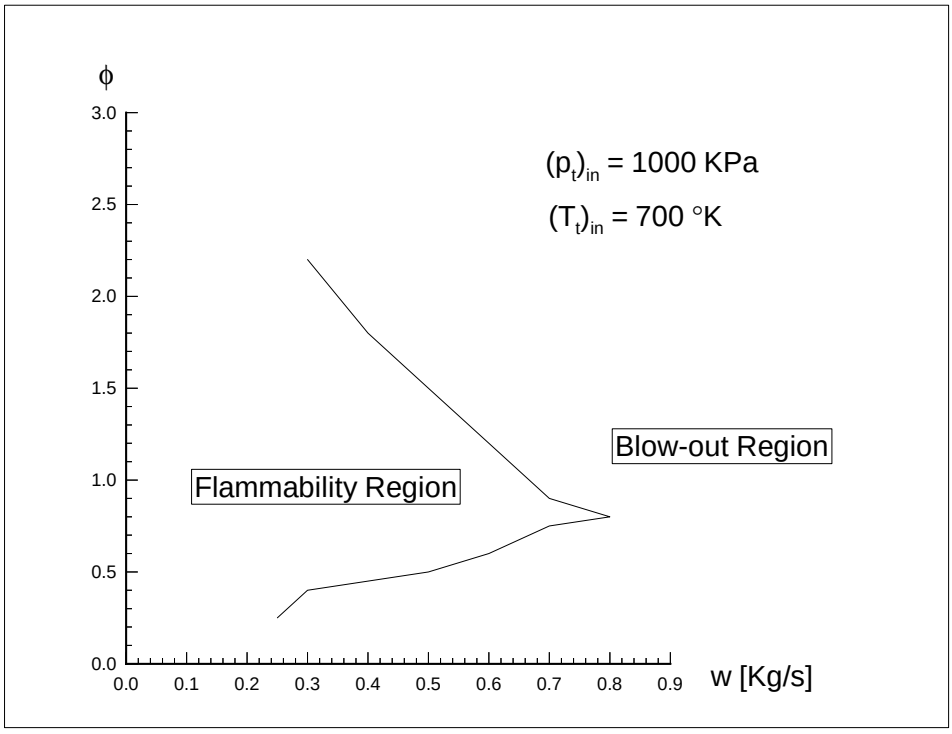

Figure 4.17: Constant-area duct - Blowout limits.

The dynamic events leading to blowout can be seen in Figs. 4.18. In these figures the history of the inlet flow-rate w_{inlet} is presented for both rich and lean blowouts. Both calculations started with an initial steady-state condition roughly corresponding to w_{inlet} = 0.5 kg/s and ϕ = 1. In both cases the fuel flow-rate was suddenly changed to values beyond the limits shown in Fig 4.17 (all boundary conditions were held constant). Both converged to a steady condition with a much higher inlet flow-rate after a transient characterized by an oscillatory back-and-forth flow; the oscillations are larger for the rich blowout. The reason behind these oscillations is that, for constant boundary conditions, the blowout process results in a reduction in the heat-release due to chemical reaction. This in turn reduces the load or pressure-loss within the domain, allowing a greater flow of air into the duct. The greater air flow-rate brings the overall mixture composition back to the stability region (before the flame leaves the duct), resulting in “reignition” and repetition of the whole process. While this process goes on the flame steadily moves towards the exit. When the flame finally leaves the domain, the oscillations die down. The transient is more violent for the rich blowout because the heat-release being added and subtracted every time is greater than for the lean case.

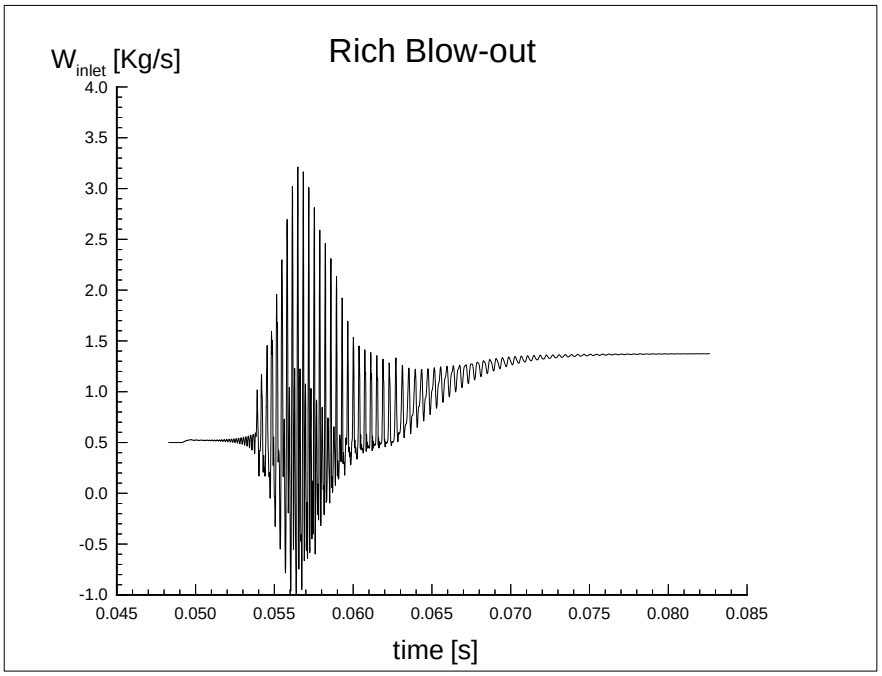

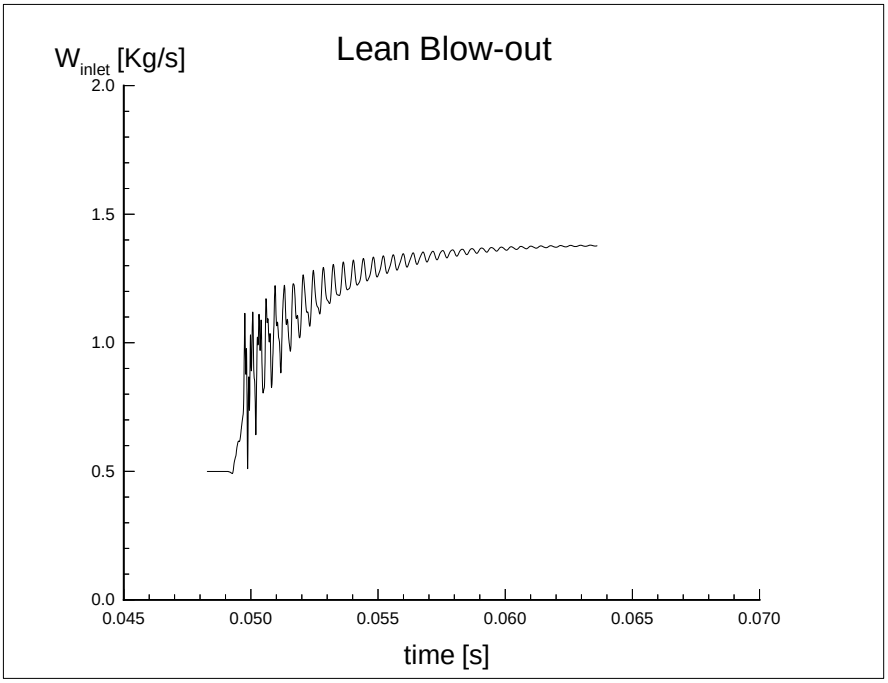

Figure 4.18: Constant-area duct - Rich and lean blowouts.

4.2.2. Perturbations in Boundary and Operating Conditions

The reverse-flow combustor shown in Fig. 4.13 was subjected to perturbations in boundary and operating conditions. More specifically, starting from the steady-state conditions reported in Section 4.1.3, oscillations were introduced separately to the fuel flow-rate and the inlet total pressure in order to determine the ability of the model to respond to controlled dynamic events.

Figure 4.19 shows the oscillations imposed on the fuel flow-rate: 50% above and below the steady-state flow-rate, at a frequency of 100 Hz. Figures 4.20 and 4.21 register the effects of these oscillations in the mass flow-rates and temperatures in the combustor respectively (refer to Fig. 4.13). As the fuel increases from a lean steady-state condition, so does the heat release and therefore the load on the combustor, reducing the entire flow-rate; the decrease in fuel has obviously opposite effects. There is an upper-limit in the heat-release though, corresponding to stoichiometric conditions; for this reason the maximum amplitude of the temperature appears to reach a ceiling at approximately the maximum adiabatic temperature. The effects of these changes in the combustor and primary-flow inlets are almost simultaneous. This can be attributed to the upper-liner dilution flow-rate which links the combustor inlet to the primary zone; its magnitude is almost as that at the inlet of the primary.

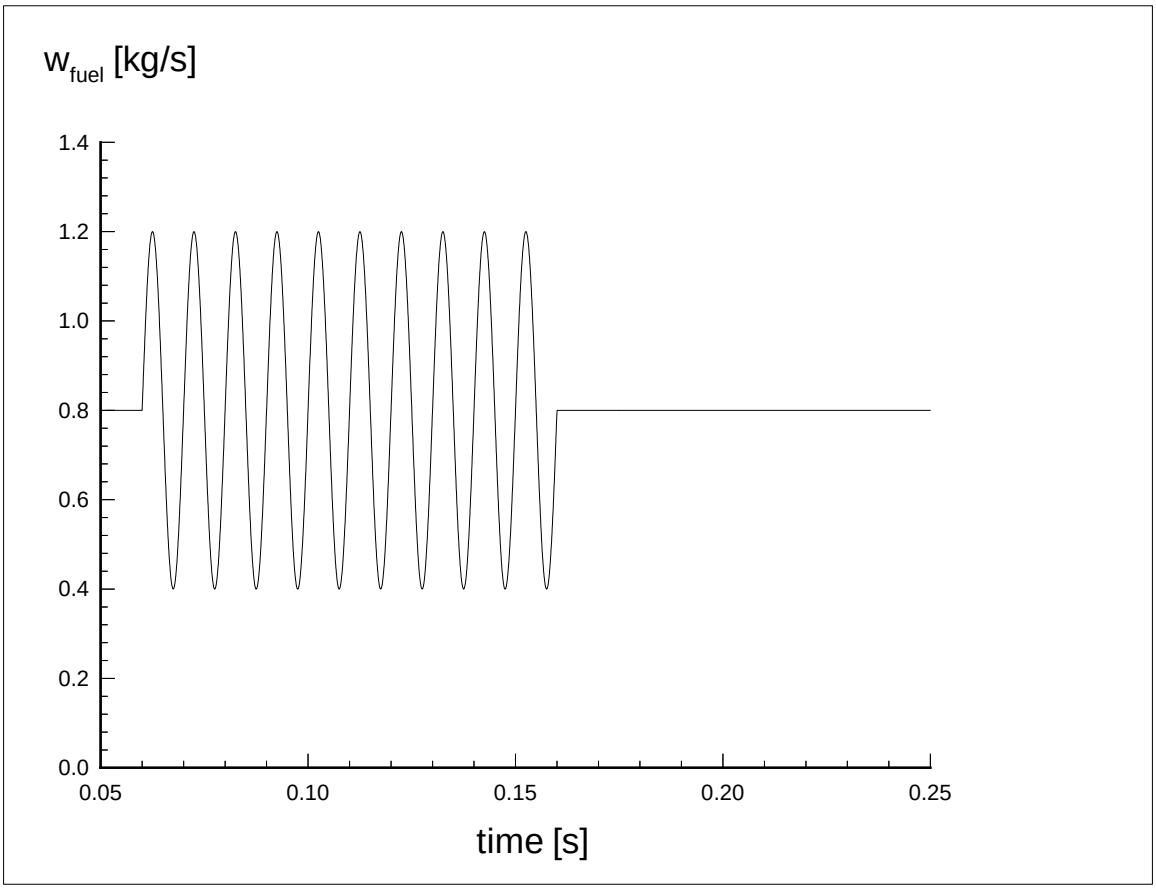

Figure 4.19: Oscillations in fuel flow-rate - Fuel input function.

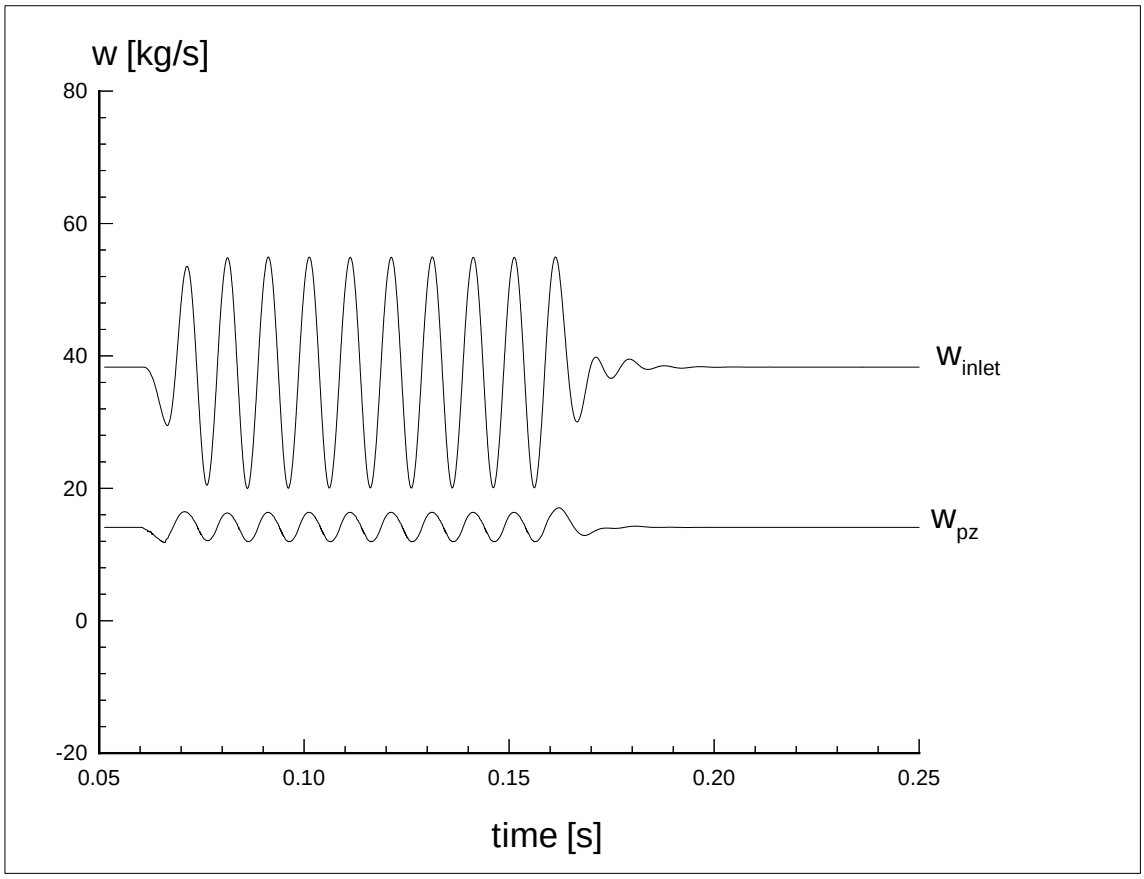

Figure 4.20: Oscillations in fuel flow-rate - Effects in mass flow-rates.

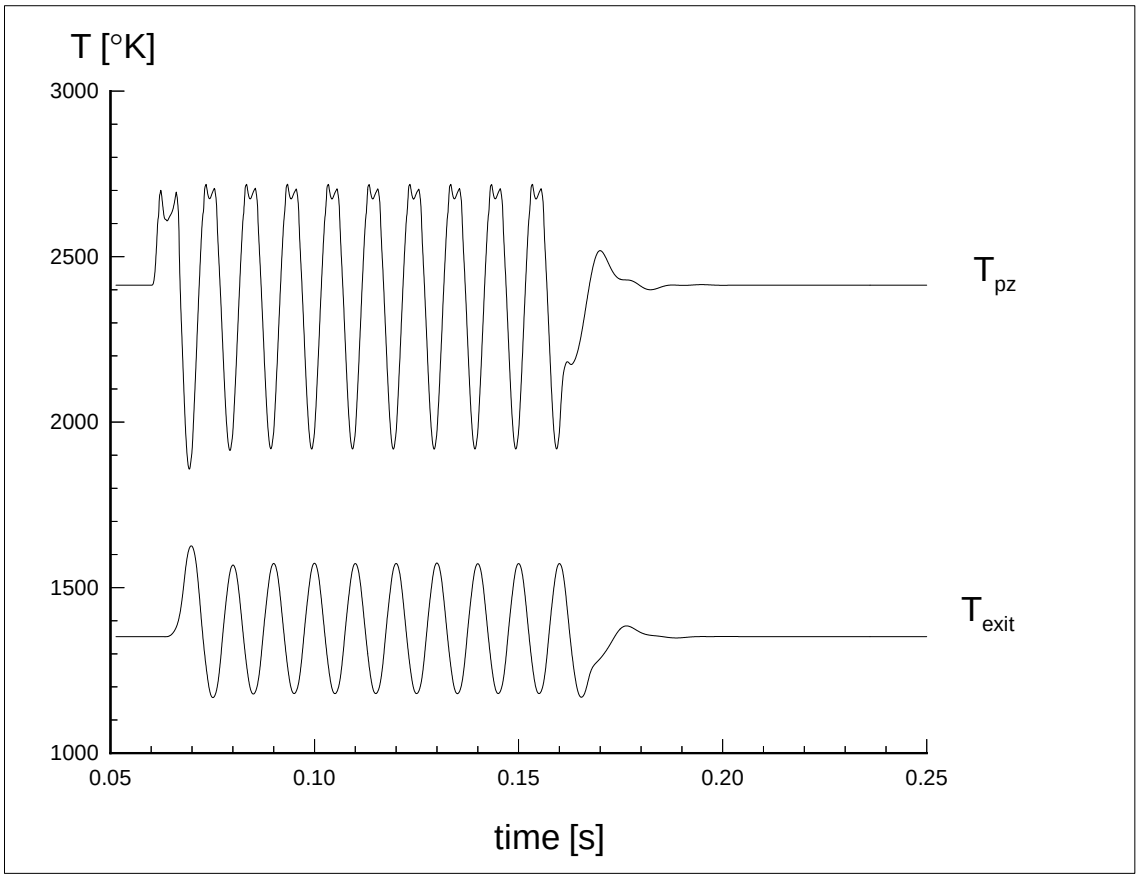

Figure 4.21: Oscillations in fuel flow-rate - Effects in temperatures.

The oscillations in inlet total pressure and its effects are shown in Fig 4.22-4.24. These oscillations are of magnitude 50% above and below the steady-state value and with a frequency of 50 Hz. The main effect of the pressure rise is to increase the flow-rate into the combustor (at constant exit pressure), reducing the overall equivalence ratio and therefore the heat-release and temperature; the opposite occurs during the downward part of the cycle. These effects are felt immediately at the inlet of the combustor, but with some delay (about a quarter cycle) at the primary inlet. Note that in this case there is flow reversal at the combustor inlet. This situation is handled by the model as if the inlet were an "exit": the imposed total pressure becomes static pressure and all the other variables are extrapolated from the interior. The delay or inertia mentioned above may account for the fact that there is still some flow into the primary even when the inlet flow is reversed. This may also explain the asymmetry in the exit temperature.

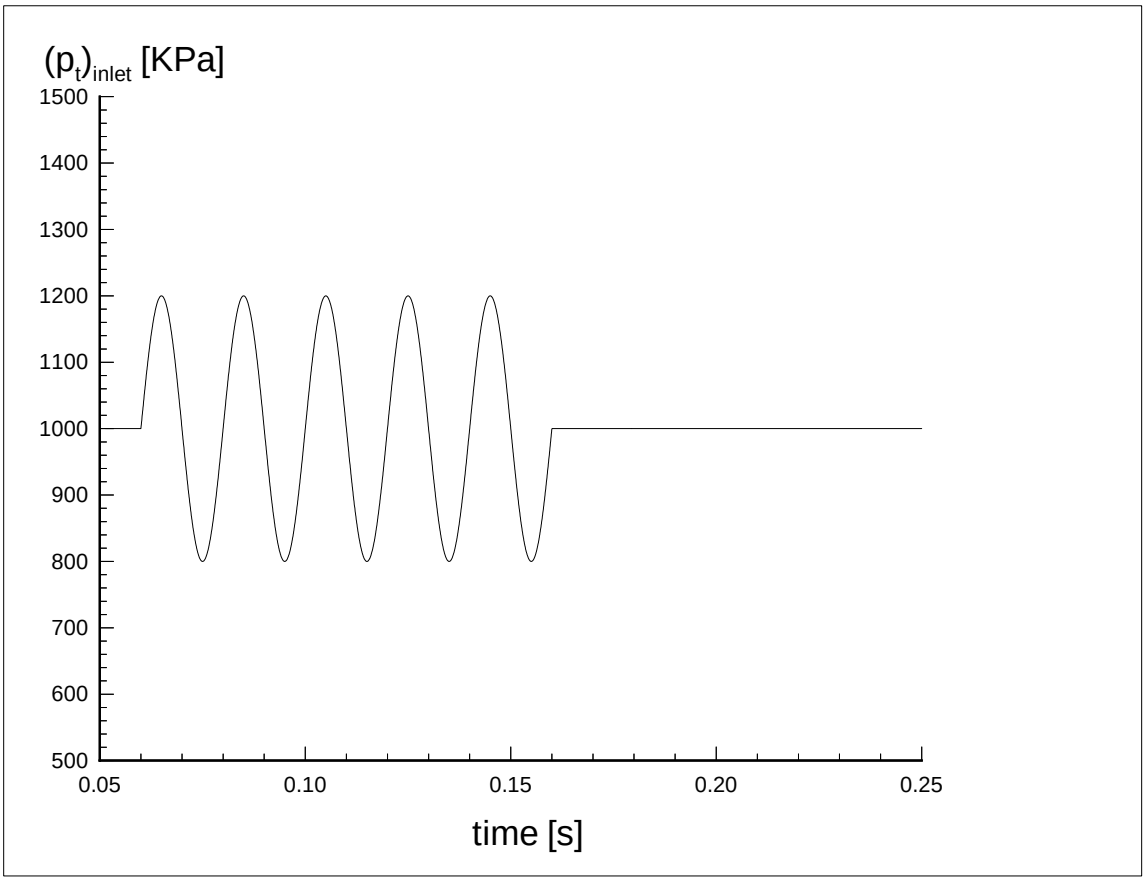

Figure 4.22: Oscillations in inlet total-pressure - Inlet total-pressure function.

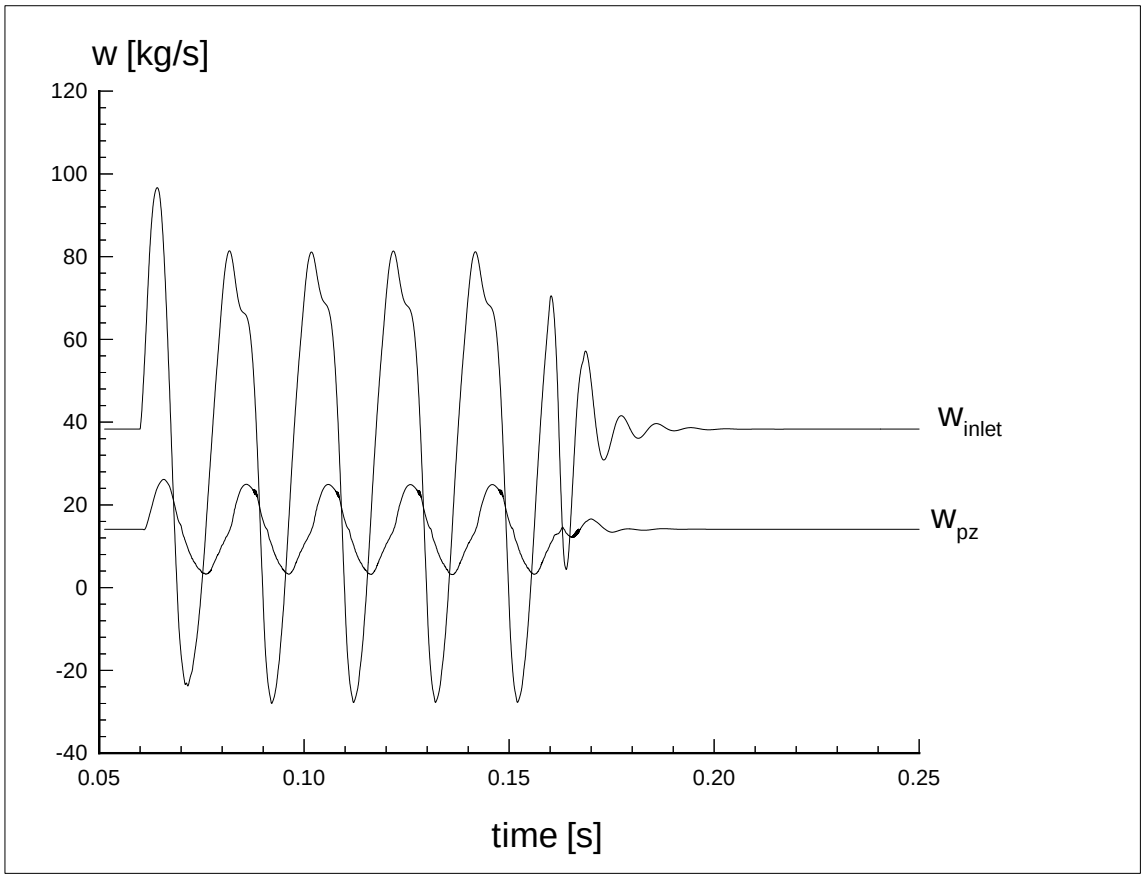

Figure 4.23: Oscillations in inlet total-pressure - Effects in mass flow-rates.

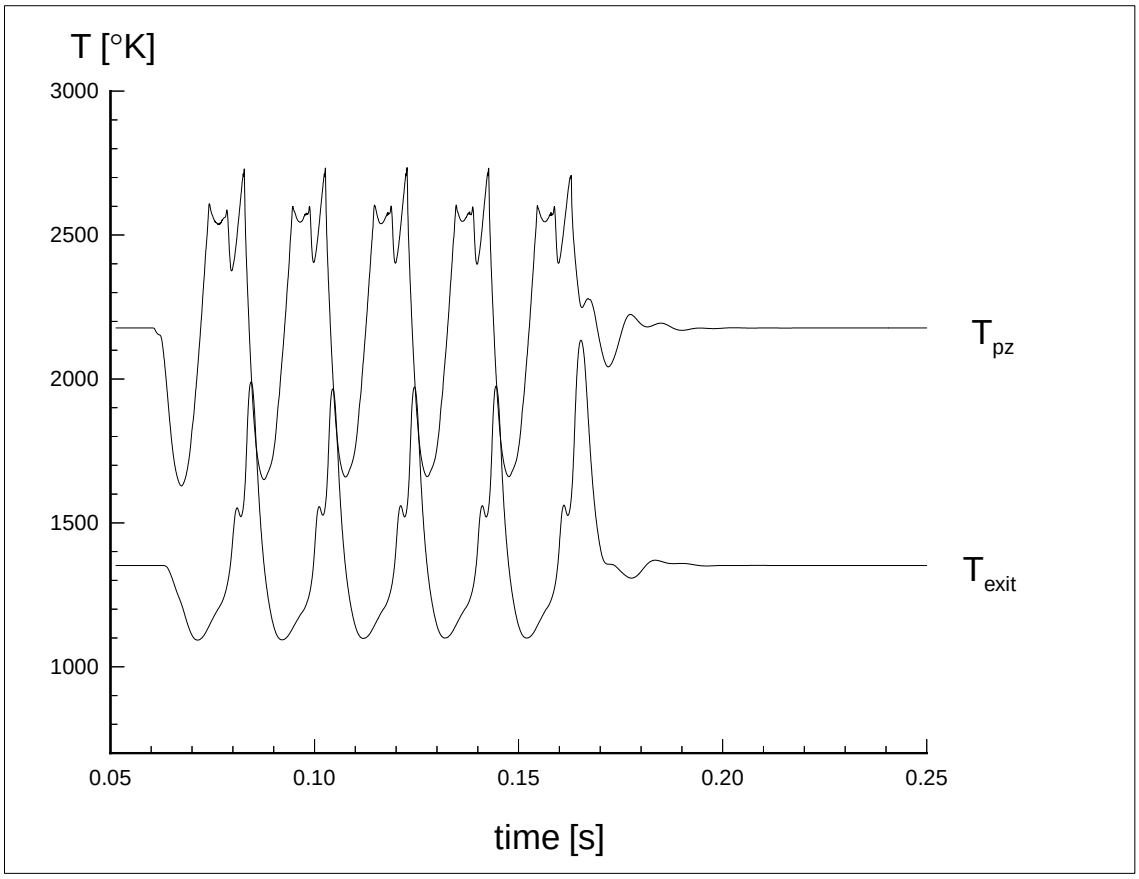

Figure 4.24: Oscillations in inlet total-pressure - Effects in temperatures.